

Hybrid broadband conduction and amplitude-driven topological confinement of sound via synthetic acoustic crystals

¹*Mathieu Padlewski,¹ Xinxin Guo,¹
Maxime Volery,¹ Romain Fleury^{2, 1} Hervé Lissek

¹Signal Processing Laboratory 2 , Ecole Polytechnique Fédérale de Lausanne,
Route Cantonale, 1015, Lausanne, Switzerland

¹Laboratory of Wave Engineering , Ecole Polytechnique Fédérale de Lausanne,
Route Cantonale, 1015, Lausanne, Switzerland

*To whom correspondence should be addressed; E-mail: mathieu.padlewski@epfl.ch

Precise wave manipulation has undoubtedly forged the technological landscape we thrive in today. Although our understanding of wave phenomena has come a long way since the earliest observations of desert dunes or ocean waves, the unimpeded development of mathematics has enabled ever more complex and exotic physical phenomena to be comprehensively described. Here, we take wave manipulation a step further by introducing an unprecedented synthetic acoustic crystal capable of realizing simultaneous linear broadband conduction and nonlinear topological insulation, depicting a robust amplitude-dependent mode localized deep within - i.e. an amplitude-driven topological confinement of sound. The latter is achieved by means of an open acoustic waveguide lined with a chain of nonlocally and nonlinearly coupled active electroacoustic resonators. Starting from a comprehensive topological model for

classical waves, we demonstrate that different topological regimes can be accessed by increasing driving amplitude and that topological robustness against coupling disorder is a direct consequence of symmetric and simultaneous response between coupled resonators. Theoretical predictions are validated by a fully programmable experimental apparatus capable of realizing the real-time manipulation of metacrystal properties. In all, our results provide a solid foundation for future research in the design and manipulation of classical waves in artificial materials involving nonlinearity, nonlocality, and non-hermiticity.

In recent decades, the study of topological systems has spread across the many fields of physics (1). Besides enabling complex wave phenomena to be elegantly described by means of simple geometric arguments, topology most notably owes its surge of interest to its remarkable resiliency against defects and parametric perturbations - a coveted feature in a world webbed by endless backscattering-sensitive communication and power lines. While there is a plethora of inquires regarding topology, these have been largely addressed in the scope of linear physics. The tendency of describing physical phenomena in linear terms is usually not a manifestation of oversight but rather of convenience - both theoretically and experimentally. Yet nonlinearity, when properly tamed, can lead to spectacular applications such as ultra directional sound sources using parametric arrays (2), energy harvesting of vorticies generated by wind turbine blades (3) and non-reciprocal transmission (4) to name a few.

Regarding nonlinear topology however, the mere scarcity of natural topologically-inclined systems within the quantum realm has encouraged scientists to develop a zoo of artificial structures, i.e. metamaterials, in view of tackling the matter from a more practical angle. These encompass a range of physical systems, including variable capacitance diodes integrated into electrical circuits (5–9), optical materials that exhibit intensity-dependent refractive indices (10–13), geometrically engineered (14, 15) or non-linearly stiff mechanical structures (16–18), and even

active components that allow nonlinearity and non-hermiticity straightforwardly (19–21).

Despite this diversity, previous surveys have revealed a clear tendency in the types of nonlinearities studied. In particular, Kerr-like on-site nonlinearities (6, 7, 10, 11, 13, 16, 18, 22–30) have dominated the landscape due to their ease of passive realization and their connection to the quantum nonlinear Schrodinger equation (31, 32).

Another trend is made evident by noticing that a majority of these synthetic topological insulators are often tailored to emulate tight-binding quantum systems which, contrary to classical waves, evolve according to Schrodinger’s equation (33). Workarounds typically involve choosing evanescently coupled lattice elements and invoking a coupled mode theory which can be straightforwardly mapped to the Schrodinger equation. Despite the convenience of such a bold cut, these systems completely oversee collective far-field scattering events, which arguably offer a far more faithful depiction of real condensed-matter systems and a deeper outreach in the search of ever more exotic properties. To date, some far-field scattering and locally resonant acoustic metamaterials have been shown to host topological interface states but all remain limited to linear descriptions (34–38). Still, even with a classical system of nonlinearly and far-field coupled scatterers, the question remains of how to assess potential topological regimes - let alone imagine an experimental realization.

We propose to address this question by means of an electronically tunable chain of coupled active electroacoustic resonators (AERs) capable of realizing real-time manipulation of crystal properties such as local resonances and nonlocal interactions. By introducing nonlinear couplings via active control, we are able to reliably generate robust amplitude-dependent topological interface states in a broad spectrum of programmable configurations at arbitrarily low pressure amplitudes. As the source amplitude increases, the dispersionless waveguide undergoes an amplitude-driven topological transition where deep bulk modes get confined to an interface as shown in a simulation presented in Figure 1 (see Methods). Starting from a clas-

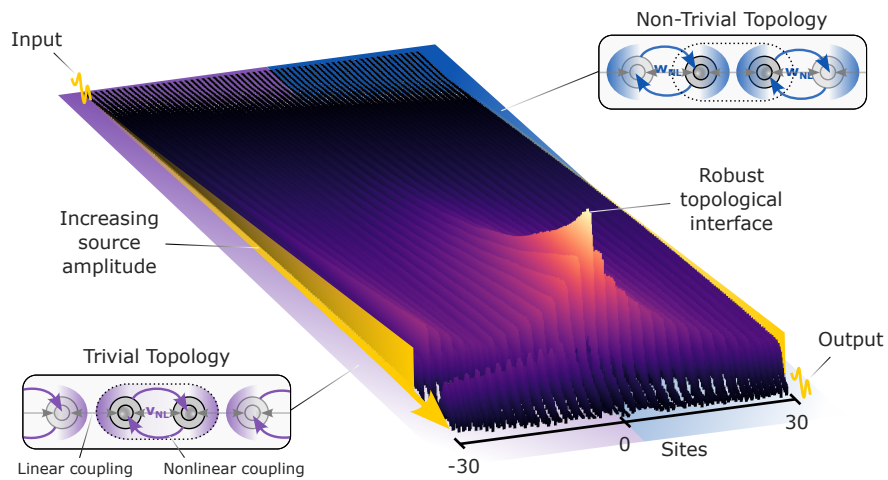


Figure 1: **Hybrid linear conduction and amplitude-driven topological confinement.** Two finite chains (30 unit cells) with distinct topology form an interface at the centre. The insets specify the topological configuration of each side - trivial topology on the left (purple) or non-trivial topology on the right (blue). Grey arrows indicate linear coupling between the equally-spaced acoustic scatterers while the purple and blue arrows correspond to intra- and inter-cell couplings v_{NL} and w_{NL} respectively. The corresponding topological mode is input at the left of the chain for increasing source amplitudes. The equal-linear couplings lead to unimpeded conduction throughout the chain whereas the dimerizing nonlinear couplings cause the appearance of an amplitude-dependant topological interface mode at the center that is robust to disorder.

sical scattering wave description, we first demonstrate that the complex resonator chain can be studied within a framework similar to that offered by standard quantum scattering theory from which a simple topological model can be derived. The predicted robust amplitude-dependant topological interface states and chiral-symmetry protection are checked against the behaviors of an analogical acoustic circuit model which faithfully captures temporal dynamics and, of course, the fully operational experimental active acoustic metacrystal.

Hamiltonian description of nonlocally-coupled chain of classical resonators

Within the monomode regime, an acoustic scattering chain of dimers with (non)linear *intra*-cell and *inter*-cell couplings, $v_{(N)L}$ and $w_{(N)L}$ respectively, can be described using the dimer state $|\Psi_n\rangle = [a_n, b_n]^T$, where a_n (b_n) is the complex pressure on the n^{th} dimer of sublattice A (B) (Fig. 2a). Its evolution is faithfully captured by the discretized wave equation (- see Methods for details),

$$(\Delta_n + \mathbf{V}_n) |\Psi_n\rangle + \mathbf{W}_{n-1} |\Psi_{n-1}\rangle + \mathbf{W}_{n+1} |\Psi_{n+1}\rangle = \Delta_t |\Psi_n\rangle \quad (1)$$

where:

$$\begin{aligned} \Delta_n &= \begin{bmatrix} \nabla_n^2 & 0 \\ 0 & \nabla_n^2 \end{bmatrix}, \Delta_t = \begin{bmatrix} c^{-2} \nabla_t^2 & 0 \\ 0 & c^{-2} \nabla_t^2 \end{bmatrix} \\ \mathbf{V}_n &= \begin{bmatrix} 0 & \check{v}(b_n) \\ \check{v}(a_n) & 0 \end{bmatrix}, \mathbf{W}_{n-1} = \begin{bmatrix} 0 & \check{w}(b_{n-1}) \\ 0 & 0 \end{bmatrix}, \mathbf{W}_{n+1} = \begin{bmatrix} 0 & 0 \\ \check{w}(a_{n+1}) & 0 \end{bmatrix} \\ \check{v}(x_n) &:= v_L + v_{NL}|x_n|^\nu, \quad \check{w}(x_n) := w_L + w_{NL}|x_n|^\nu, \quad x_n \in [a_n, b_n] \end{aligned}$$

For sufficiently weak nonlinearity of order ν , (namely $v_{NL} \ll v_L$ and $w_{NL} \ll w_L$), the modal solution can be approximated to that of a time-harmonic Bloch wave $|\Psi_n\rangle = e^{i(q(na) - \omega t)} |\Psi_0\rangle$ which, substituted into Eq.(1), yields the following familiar eigenvalue problem,

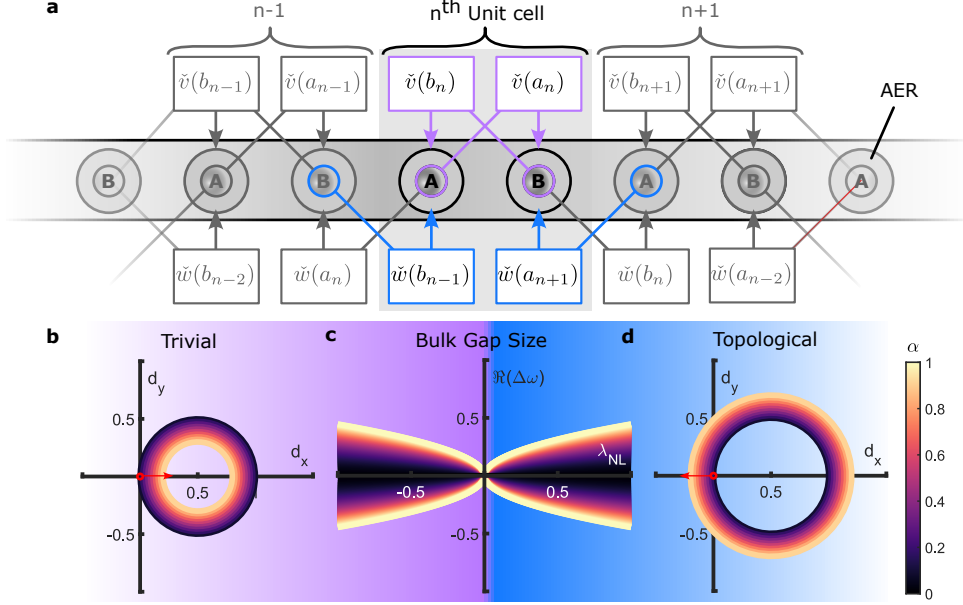


Figure 2: **Theoretical model for nonlinear topology.** **a** Coupling scheme for chain of nonlinearly dimerized scatterers. Two AERs labelled A and B constitute the unitcell. Intra- and inter-cell couplings (purple and blue arrows resp.) are conveyed by nonlinear amplitude-dependant parameters $\check{v}(p_n) := v_L + v_{NL}|p_n|^\nu$ and $\check{w}(p_n) := w_L + w_{NL}|p_n|^\nu$ where $p_n = a_n, b_n$ is the pressure on site A, B of the n -th dimer respectively. **b-d** Amplitude-driven topological transition for equal linear coupling $v_L = w_L$ and where nonlinear couplings specify the topological regime. We define the nonlinear dimerization parameter $\lambda_{NL} = w_{NL} - v_{NL}$ where $w_{NL} + v_{NL} = 1$. **b** Trivial nonlinear coupling ($\lambda_{NL} < 0$): Endpoint path of the d -vector representing the Hamiltonian, $\mathbf{H} = \mathbf{d}(q, \alpha) \cdot \boldsymbol{\sigma}$, for increasing dimer amplitude α . **c** Bulk gap size as a function of dimer amplitude α and the nonlinear dimerization parameter λ_{NL} . **d** Topological nonlinear coupling ($\lambda_{NL} > 0$): Endpoint path of the d -vector for increasing dimer amplitude α .

$$\mathbf{H}|\Psi_0\rangle = \left(\frac{\bar{\omega}}{c}\right)^2 |\Psi_0\rangle \quad (2)$$

where

$$\mathbf{H} = \underbrace{\begin{bmatrix} 0 & v_L + w_L e^{+iqa} \\ v_L + w_L e^{-iqa} & 0 \end{bmatrix}}_{\mathbf{H}_L} + \underbrace{\begin{bmatrix} 0 & (v_{NL} + w_{NL} e^{+iqa})|b_0|^\nu \\ (v_{NL} + w_{NL} e^{-iqa})|a_0|^\nu & 0 \end{bmatrix}}_{\mathbf{H}_{NL}} \quad (3)$$

and

$$\left(\frac{\bar{\omega}}{c}\right)^2 := \left(\frac{\omega}{c}\right)^2 - \frac{2}{a^2}(\cos(qa) + 1)$$

Note that $|a_0|$ and $|b_0|$ correspond to the extended Bloch-wave amplitudes at sites A and B within the unit cell. The pseudo-hamiltonian \mathbf{H} , composed of linearly and nonlinearly-coupled parts \mathbf{H}_L and \mathbf{H}_{NL} , closely resembles that of a Schrodinger system from condensed matter or photonics. In fact, for $\mathbf{H}_{NL} = 0$, \mathbf{H} directly maps to the Su-Schrieffer-Heeger model (39), albeit with wave-states corresponding to pressure modal amplitudes and the pseudo-eigenenergy that is quadratic in frequency. Indeed, first degree eigenvalues of a quantum Hamiltonian fundamentally originate from the first order time differential operator in the Schrodinger equation whereas here, the system is described by the wave equation which is second order in time. One could argue that \mathbf{H} describes a generalized Schrodinger system.

Nonlinear topological model of a scattering chain

We now aim to find a topological invariant for \mathbf{H} . One strategy is to map \mathbf{H} to a closed-path in some Riemannian manifold and to define a topological invariant based on geometric arguments. Expressing \mathbf{H} ((3)) in terms of Pauli matrices would offer a promising pathway but

the amplitude-dependent terms $|a_0|$ and $|b_0|$ in \mathbf{H}_{NL} render it non-hermitian and consequently non-Pauli-decomposable. The latter is simply overcome by imposing equal linear couplings which leads to neighboring amplitudes to being approximately equal: i.e. $v_L = w_L \Rightarrow |a_0| \approx |b_0|$ (details in Supplementary Material). Consequently, the pseudo-hamiltonian $\mathbf{H} = \mathbf{H}_L + \mathbf{H}_{\text{NL}}$ can completely be written in terms of Pauli matrices σ :

$$\mathbf{H} = \underbrace{(d_{x,L}(q) + d_{y,NL}(q, \alpha))}_{d_x(q, \alpha)} \sigma_x + \underbrace{(d_{y,L}(q) + d_{x,NL}(q, \alpha))}_{d_y(q, \alpha)} \sigma_y$$

where $[d_{x,L}, d_{y,L}] = [v_L(1 + \cos(qa)), w_L \sin(qa)]$ with $v_L = w_L$, $[d_{x,NL}, d_{y,NL}] = [(v_{NL} + w_{NL} \cos(qa))\alpha^\nu, w_{NL} \sin(qa)\alpha^\nu]$ and $\alpha = (|a_0|^\nu + |b_0|^\nu)^{1/\nu}$ is the dimer mode amplitude. \mathbf{H} is thus mapped to a circle in the (d_x, d_y) plane and is equipped with a dimer mode amplitude-dependant radius. Note that the system is now partitioned into two distinct channels that operate in parallel: a permanent conducting channel assured by linear couplings and an amplitude-dependant insulating channel by nonlinear coupling. Fig. 2b and Fig. 2d show amplitude-driven transitions to trivial or to topological regimes respectively for equal linear coupling $v_L = w_L$ depending on the nonlinear coupling configuration. The topological invariant is 0 if $\mathbf{d}(q, \alpha)$ encircles the origin and 1 otherwise. The latter is also straightforwardly defined by the winding number $W = \frac{1}{2\pi i} \int_{-\pi}^{\pi} \frac{d}{dq} \ln(d_x(q, \alpha) - id_y(q, \alpha)) dq$ (40). The pseudo-frequency band gap computed near the edges of the Brillouin zone, $\Delta\bar{\omega} = \pm c\sqrt{|(v_{NL} - w_{NL})\alpha^\nu/2|}$ (c.f. Supplementary Material), opens for non-equal nonlinear couplings and widens with increasing amplitude α as shown in Fig. 2c.

Finally, this system owes its topological protection to symmetric temporal coupling which translates to chiral symmetry of \mathbf{H} . In practice, topological protection is lost if a phase shift $\Delta\omega t$ is introduced in the Bloch-wave solution, $|\Psi_0\rangle = [a_0, e^{i\Delta\omega t} b_0]^T$ which alters the eigenvalue problem (2) to

$$\begin{aligned} & \left[\begin{array}{cc} +d_z & \check{v}(b_0) + \check{w}(b_0)e^{+iqa} \\ \check{v}(a_0) + \check{w}(a_0)e^{-iqa} & -d_z \end{array} \right] |\Psi_0\rangle = \\ & \left(\left(\frac{\bar{\omega}}{c} \right)^2 + d_z \right) |\Psi_0\rangle \end{aligned} \quad (4)$$

where $d_z = \frac{1}{2}(\Delta\omega/c)^2$.

The new diagonal elements appearing in the pseudo-hamiltonian correspond to a non-trivial Pauli-Z component, d_z , and consequently break the topology-protecting chiral symmetry.

Experimental validations

Realization of amplitude-dependant interface modes

Amplitude-dependant interface modes are experimentally realized, closely matching theoretical predictions. A finite metacrystal composed of 16 individually-controlled AERs was successfully developed and manufactured - the details of which are found in the Methods. A comprehensive overview of the experimental apparatus is presented detailing the electronic coupling scheme, the unit cell and the coupling configuration of the metacrystal (Figs 3a-c). The first half of the crystal is electronically configured such as to favor nonlinear intra-cell coupling, i.e. $v_{NL} > w_{NL}$, and the other to favor inter-cell coupling, $v_{NL} < w_{NL}$. In other words, the system is set to host a topological interface state at the center of the metacrystal. Equal linear couplings are achieved without the need of active control as its assured passively by the equal spacing of the AERs along the duct. Nonlocal and nonlinear couplings, on the other hand, are arbitrarily set to third order and achieved by means of an active feedback loop as explained in Figure 3a. This nonlinearity corresponds to $\nu = 2$ in the aforementioned topological model and resembles a "Kerr-like coupling" configuration in a Schrodinger description. Note that the coupling strengths from site to site are chosen symmetrical but can easily be modified to obtain non-reciprocity which will be at the heart of a future study. The topological interface mode is

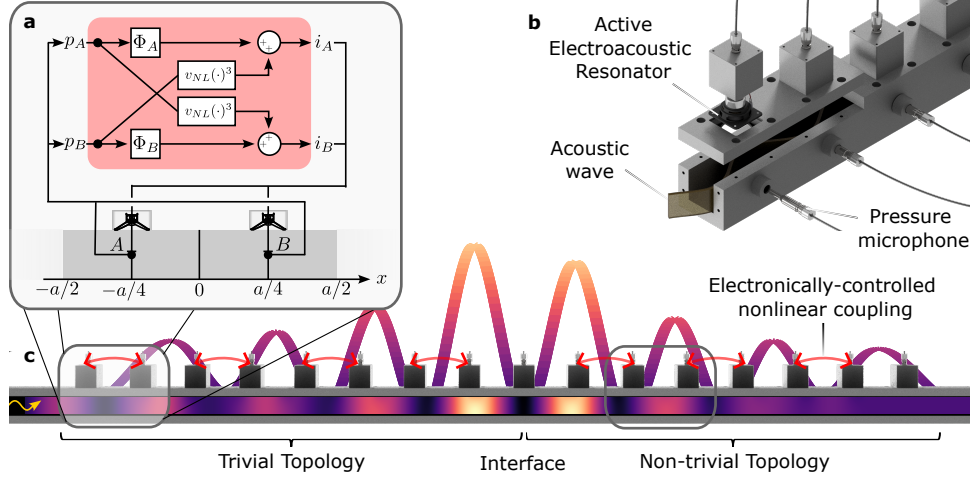


Figure 3: **Experimental apparatus and coupling scheme.** **a** Controlling nonlinear coupling in a unit cell. The pressures $p_{A,B}$ are probed at resonators A and B and are inputted and processed in a real time by a controller highlighted in red. From left to right, the pressures are read out and follow one of two paths: The first is denoted by the $\Phi_{A,B}$ operation which corresponds to local impedance synthesis of the resonator in view of reducing local losses (c.f. Methods). The second denoted by $v_{NL}(\cdot)^3$ corresponds to the controlled nonlinear coupling operation. Finally, electrical currents $i_{A,B}$ are outputted and conveyed to their respective resonators. **b** Segment of the active experimental duct highlighting the composition of a unit cell. Pressure microphones centered at the AERs serve both as real-time interaction control and mode probing (- in phase and in amplitude). **c** Cross-section of the full experimental metacrystal where the absolute pressure in the duct (also represented in the background) illustrates an interface mode driven at high amplitude excitations. The electronically coupled pairs along the chain (red arrows) are configured such as to favor intra-cell coupling on one side and inter-cell coupling on the other. The unit cell, indicated on both sides by the grey rectangles, highlight the different topological configurations.

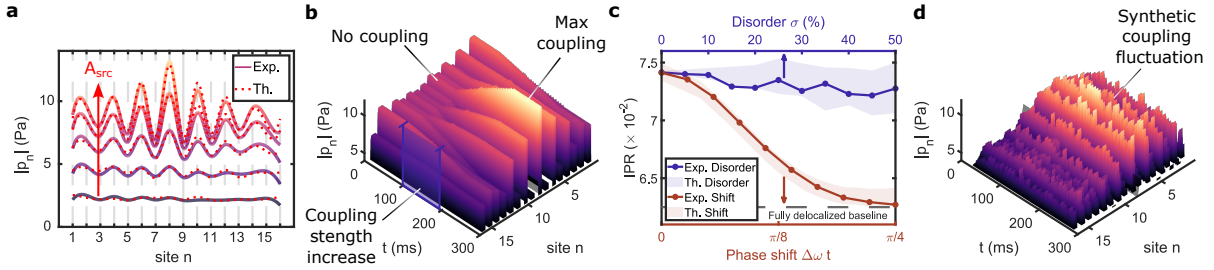


Figure 4: Realization of robust amplitude driven topological interface via tunable active control. **a** Amplitude-driven topological interface state. Pressure is measured at each site along the duct and plotted for five different source amplitudes for both experimental (thick colored) and theoretical dynamics (dashed red line). **b** Real-time experimental parameter tuning. Experimental spatio-temporal evolution of the pressure at each site showcasing the emergence of a topological interface state due to an adiabatic temporal increase of the nonlinear electronic coupling strength at the region highlighted in blue for a fixed source amplitude. **c** Topological robustness assessment. The inverse participation ratio is computed for both experimental (line) and theoretical (shaded interval) dynamics as a function of coupling disorder σ (blue) and phase shift $\Delta\omega t$ representing a delay between the coupling responses of adjacent sites (red). The shaded interval corresponds to the maximum and minimum limits obtained over 20 simulations with different random coupling configurations. **d** Robustness to coupling fluctuation. Experimental spatio-temporal evolution of the pressure at each site showing the robustness of the topological interface in presence of fluctuating disorder ($\langle\sigma\rangle_t = 50\%$) which is analogous to temperature in condensed matter systems.

depicted by driving the source resonator at 635 Hz which corresponds to the Bragg frequency and by subsequently measuring the pressure at each AER. The modes are plotted for increasing levels of source amplitude A_{src} both from experimental and theoretical temporal dynamics as presented in Figure 4a. The latter provides clear experimental evidence of a rising topological interface mode profile as the source amplitude is increased and is well supported by the temporal dynamics simulation (see Methods for simulation details). It can also be noted that nearly identical pressure values on each extremities of the metacrystal is a manifestation of the underlying broadband conducting channels assured by the equal linear couplings. Minute transmission loss is explained by the mechanical resistance of the AERs and by thermoviscous losses in the waveguide.

While the effect of nonlinearity is simply demonstrated by increasing the source amplitude, we stress that it is not a manifestation of gain saturation. On the contrary, the nonlinearity here is well defined and the localization of the interface state only depends on the balance between the electronic coupling strength and the source amplitude. To illustrate this, the system is configured such as to increase the nonlinear coupling strength given a constant source amplitude (Fig. 4b) - a feat made possible thanks to the tunability of the experimental apparatus. A quantitative assessment of the localization achieved by computing the inverse participation ratio (IPR) as a function of the source amplitude can be found in the Supplementary Material. This dynamic coupling control will now be used to reveal the underlying symmetry protecting the topological interface mode.

Topological robustness assessment and chiral-symmetry breaking

One of the key phenomenological markers asserting a claimed topological state is its protection against system disorder. In multiple scattering systems, protection has been shown to be a direct consequence of symmetry constraints of the unit cell transfer matrix M_{cell} - namely time-

reversal symmetry and $M_{\text{cell}}^2 = 1$ (35). Here, as the scattering system has been expressed in terms of a pseudo-hamiltonian \mathbf{H} , the symmetry protection is translated to the chiral symmetry of \mathbf{H} i.e. $\sigma_z \mathbf{H} \sigma_z^\dagger = -\mathbf{H}$, where $\sigma_z = [1, 0; 0, -1]$. The goal is thus to demonstrate topological robustness against coupling disorder and that chiral protection, assured here by time-reversal symmetry, can be broken by introducing a so-called phase shift between the coupled sites.

The robustness can be assessed by measuring localization as a function of system disorder. As mentioned before, the IPR quantifies localization and here, $\text{IPR} = \sum_{i=1}^{16} (|\bar{p}_i|^2)^2$ where \bar{p}_i is the normalized pressure at site i such that $\sum_{i=1}^{16} |\bar{p}_i|^2 = 1$. The smallest value of IPR corresponds to a fully delocalized state, $|\bar{p}_i| = 1/\sqrt{16} \forall i \Rightarrow \text{IPR} = 1/16$. Conversely, the largest value of the IPR is obtained for a perfectly localized state at site i_0 , $|\bar{p}_i| = \delta_{i,i_0} \Rightarrow \text{IPR} = 1$.

The coupling disorder strength σ is defined as a random deviation of the couplings with respect to their nominal values. The IPRs extracted from both theoretical and experimental dynamics (and averaged over 20 random coupling configurations) are plotted as a function of σ in Figure 4c (blue).

Time-reversal symmetry is preserved as long as coupling is simultaneous - i.e. the unidirectional non-local coupling from site A to site B occurs at the same time as the coupling from B to A . This temporal symmetry can be trivially broken by introducing a delay or phase shift $\Delta\omega t$ between the unidirectional couplings of adjacent sites, say by adding a tuneable time delay block after the current output i_A in Figure 3a. Again, the IPRs are extracted from both theoretical and experimental dynamics and plotted as a function of $\Delta\omega t$ in Figure 4c (red).

The results indicate remarkable robustness to disorder which is indicated by a constant IPR as a function of coupling disorder. Notice that robustness remains present for coupling disorders nearing 50% of their nominal values. Furthermore, Figure 4d shows that the nonlinear topological interface state remains well defined even when real-time fluctuating disorder is introduced ($\langle\sigma\rangle_t = 50\%$). Indeed, the disorder updates after every feedback cycle and is reminiscent of

lattice temperature in condensed matter. On the other hand, delaying the coupling response via $\Delta\omega t$ dramatically hinders the stability of the localized interface state as indicated by the rapid IPR drop with increasing shift. The delay effectively breaks time-reversal symmetry and, as predicted in (4), introduces a non-trivial d_z component leaving the system topology ill-defined.

Discussion

In this study, we have shown that it is possible to confine an amplitude-driven topological mode deep within a structured system all while maintaining broadband conduction from edge to edge. In other words, we presented a dual-channel metamaterial capable of achieving simultaneous linear broadband conduction and nonlinear topological insulation depicting a localized amplitude-dependant mode at an interface. For a system solely dimerized by nonlinear couplings, a topological model is rigorously derived from the classical wave equation predicting the presence of topological states protected by chiral symmetry. The amplitude-dependency, the robustness and its protecting symmetry all have been validated by both temporal dynamics simulations and a highly configurable experimental apparatus composed of individually-controlled active electroacoustic resonators. Practical implementations of the latter developments are vast: Non-perturbative waveguide intensity probing, direct mapping of physical systems such as Dirac and Klein-Gordon particles in one-dimensional periodic potentials (41), the realization of exotic topological Floquet systems using time-varying potentials and the study of non-reciprocal topology by asymmetric coupling strength - all of which are simply implementable thanks to the electronic configurability offered by the experimental apparatus.

Methods

Active acoustic crystal design and control scheme

The acoustic waveguide is composed of CNC-milled 20mm thick PVC slabs lined with 16 off-the-shelf Visaton FRWS 5 - 8 Ohm drivers, 3D-printed back-cavities, and quarter-inch PCB microphones. The pressure microphones centered at the AERs (Fig. 3b) serve both for interaction control and mode probing. Active control is carried out by a commercial Speedgoat machine equipped with the IO135 module. This Direct Memory Access (DMA) module enables both on-site tunability and low-latency driver control over all 16 channels. COMSOL Multiphysics finite element simulations were performed enabling design optimization and experimental validation for linear coupling configurations. In order to account for manufacturing inconsistencies, the mechanical mass, resistance and compliance of each speaker was characterized following methods described by E. Rivet (42) and actively tuned to match one another. Finally, the quality factor of the resonators were all enhanced by synthetically reducing AER acoustic resistance by 80%. (- details in Supplementary Material).

Hamiltonian description of a classical metamaterial

The aim here is to express a resonator chain in terms a familiar Hamiltonian formalism in view of assessing its topological properties. Let's start with the propagation of a pressure field $\psi(x, t)$ through an scattering acoustic waveguide, which, within the monomode regime, can be described by the 1D wave equation:

$$\left(\nabla_x^2 - c^{-2}\nabla_t^2\right) \psi(x, t) = F(x, t, \psi) \quad (5)$$

where F specifies intrinsic system interactions. Now consider $2N$ discrete nonlinear and nonlocal scatterers at positions $x_n, n = 0, 1, \dots, 2N$ along the waveguide. The system interac-

tions are now specified as:

$$\begin{aligned}
F(x_n, t, \psi) = & \int_{-\infty}^{+\infty} (\chi_L^- + \chi_{NL}^- |\psi(x', t)|^\nu) \delta(x' - x_n) + \\
& (\chi_L^+ + \chi_{NL}^+ |\psi(x', t)|^\nu) \delta(x' + x_n) dx' = \\
& (\chi_L^- + \chi_{NL}^- |\psi_{n-1}(t)|^\nu) \psi_{n-1}(t) + \\
& (\chi_L^+ + \chi_{NL}^+ |\psi_{n+1}(t)|^\nu) \psi_{n+1}(t)
\end{aligned} \tag{6}$$

where $\chi_{L/NL}^\pm$ correspond to the linear and nonlinear coupling strengths to the neighboring sites and $\psi(x_{n\pm 1}, t) := \psi_{n\pm 1}(t)$. In view of brevity, t is dropped from the notation. One may notice that local Lorentzian interactions capturing resonator dynamics have been conveniently left out. Indeed, this mindful omission was done in view of simplicity as it has been rigorously demonstrated that topological phenomena occurring in resonator chains arise exclusively from Bragg scattering events and not local resonances (38).

If the scatterers are equally spaced with periodicity $a/2$, i.e. $x_n = na/2$, and if the operating wavelength is larger than the unitcell size a (-subwavelength regime), the spatial differential operator ∇_x^2 can be rigorously discretized:

$$\begin{aligned}
\nabla_x^2 \psi(x) & \approx \frac{\psi(x-a) - 2\psi(x) + \psi(x+a)}{a^2} \\
& = \frac{\psi_{n-1} - 2\psi_n + \psi_{n+1}}{a^2} \\
& := \nabla_n^2 \psi_n
\end{aligned} \tag{7}$$

Using equations (5) and (7) leads to the discretized wave equation (1).

Nonlinear temporal dynamics

The aim here is to build a dynamical matrix corresponding to a N -cell acoustic scattering chain of electronically controlled resonators in view of faithfully predicting the temporal evolution of nonlinear topological modes. Local resonating dynamics can reliably be captured by means of

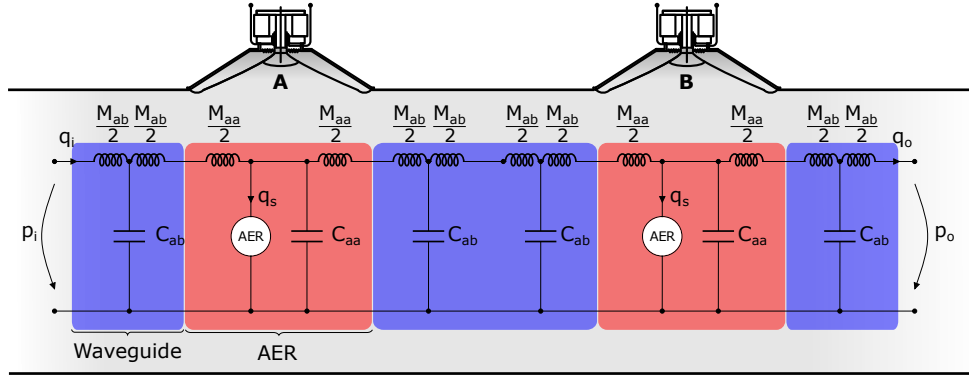


Figure 5: Scattering dynamics through a unit cell using acoustic circuit formalism. The latter specifies the relation between input and output pressures and volumetric flows, (p_i, q_i) and (p_o, q_o) respectively. Three waveguide parts and two AER parts, highlighted in blue and red respectively, are placed within the corresponding experimental unit cell schematically drawn in grey.

an equivalent circuit formalism where electrical potential and current are analogically substituted with acoustic pressure p and volumetric flow q . The electrical inductance, resistance and capacitance are respectively substitutes for the acoustic mass M_a , resistance R_a and compliance C_a . Figure 5 depicts the circuit describing an acoustic unit cell composed of a waveguide loaded with two equally spaced AERs. The circuit is partitioned into three identical waveguide and two AER parts - each of which is defined by a sub-dynamical matrix which will be elaborated below. The product of all latter five elements yields the total unit cell dynamical matrix. Table 1 summarizes the acoustic parameters used for the simulation. Note that these parameters correspond to the tuned AERs used in the experimental apparatus.

Table 1: Experimental and simulation parameters

Parameter	Symbol	Value	Unit
Ac. Mass between AERs	M_{ab}	29.0	kg/m ⁴
Ac. Compliance between AERs	C_{ab}	$7.2 \cdot 10^{-10}$	m ³ /Pa
Ac. Mass at AER	M_{aa}	23.9	kg/m ⁴
Ac. Compliance at AER	C_{aa}	$5.9 \cdot 10^{-10}$	m ³ /Pa
AER Ac. Mass	M_{as}	$4.5 \cdot 10^4$	kg/m ⁴
AER Ac. Resistance	R_{as}	463.7	Pas/m
AER Ac. Compliance	C_{as}	$3.1 \cdot 10^{-10}$	m ³ /Pa
Force Factor	Bl	1.4	Pa/A
Effective Diaphragm Area	S_d	$12 \cdot 10^{-4}$	m ²

Waveguide part:

The relation between the input and output pressures and volumetric flows in a simple waveguide section, (p_i, q_i) and (p_o, q_o) respectively, is given by the following dynamic equations:

$$\Rightarrow \begin{cases} -p_i = -\frac{M_{ab}}{2} \frac{dq_i}{dt} - \frac{1}{C_{ab}} \int (q_i - q_o) dt \\ \frac{1}{C_{ab}} \int (q_i - q_o) - \frac{M_{ab}}{2} \frac{dq_o}{dt} = p_o \end{cases}$$

The latter can be conveniently written in matrix form:

$$\Rightarrow \left\{ \begin{bmatrix} -\frac{M_{ab}}{2} & 0 \\ 0 & -\frac{M_{ab}}{2} \end{bmatrix} \frac{d^2}{dt^2} + \begin{bmatrix} -C_{ab}^{-1} & C_{ab}^{-1} \\ C_{ab}^{-1} & -C_{ab}^{-1} \end{bmatrix} \right\} \begin{bmatrix} x_i \\ x_o \end{bmatrix} = \begin{bmatrix} -p_i \\ p_o \end{bmatrix}$$

Active Electro-Acoustic Resonator part:

Similarly to the waveguide, the relation between (p_i, q_i) and (p_o, q_o) is given by the following dynamic equation:

$$\Rightarrow \begin{cases} -p_i = -\frac{M_{aa}}{2} \frac{dq_i}{dt} - \frac{1}{C_{aa}} \int (q_i - q_s - q_o) dt \\ -\hat{\zeta} q_s - \frac{Bl i}{S_d} - \frac{1}{C_{aa}} \int (q_i - q_s - q_o) dt = 0 \\ \frac{1}{C_{aa}} \int (q_i - q_s - q_o) dt = \frac{M_{aa}}{2} \frac{dq_o}{dt} + p_o \end{cases}$$

where the resonator dynamics are captured by the AER impedance operator,

$$\hat{\zeta} = M_{as} \frac{d}{dt} + R_{as} + \frac{1}{C_{aa}} \int dt$$

and the controllable electrical current i is at the root of a supplementary resonator interactions - local and non-local.

In matrix form, the latter yields:

$$\Rightarrow \left\{ \begin{array}{l} \left[\begin{array}{ccc} -\frac{M_{aa}}{2} & 0 & 0 \\ 0 & M_{as} & 0 \\ 0 & 0 & -\frac{M_{aa}}{2} \end{array} \right] \frac{d^2}{dt^2} + \left[\begin{array}{ccc} 0 & 0 & 0 \\ 0 & R_{as} & 0 \\ 0 & 0 & 0 \end{array} \right] \frac{d}{dt} + \\ \left[\begin{array}{ccc} -C_{aa}^{-1} & C_{aa}^{-1} & C_{aa}^{-1} \\ -C_{aa}^{-1} & C_{as}^{-1} + C_{aa}^{-1} & C_{aa}^{-1} \\ C_{aa}^{-1} & -C_{aa}^{-1} & -C_{aa}^{-1} \end{array} \right] \end{array} \right\} \begin{bmatrix} x_i \\ x_s \\ x_o \end{bmatrix} = \\ \begin{bmatrix} -p_i \\ 0 \\ p_o \end{bmatrix} + \begin{bmatrix} 0 \\ -\frac{Bli}{S_d} \\ 0 \end{bmatrix}$$

Unit cell dynamical matrix:

The evolution of an acoustic charge $\mathbf{x} := \int \mathbf{q} dt$ at each circuit node in Figure 5 is computed using the following dynamical system where the colored block-diagonal matrices correspond to

those used in the aforementioned waveguide and AER:

$$\left\{ \underbrace{\begin{bmatrix} \cdot & \cdot & \cdot & \cdot & \cdot & \cdot & \cdot & \cdot & \cdot \\ \cdot & \cdot & \cdot & \cdot & \cdot & \cdot & \cdot & \cdot & \cdot \\ \cdot & \cdot & \cdot & \cdot & \cdot & \cdot & \cdot & \cdot & \cdot \\ \cdot & \cdot & \cdot & \cdot & \cdot & \cdot & \cdot & \cdot & \cdot \\ \cdot & \cdot & \cdot & \cdot & \cdot & \cdot & \cdot & \cdot & \cdot \\ \cdot & \cdot & \cdot & \cdot & \cdot & \cdot & \cdot & \cdot & \cdot \\ \cdot & \cdot & \cdot & \cdot & \cdot & \cdot & \cdot & \cdot & \cdot \\ \cdot & \cdot & \cdot & \cdot & \cdot & \cdot & \cdot & \cdot & \cdot \\ \cdot & \cdot & \cdot & \cdot & \cdot & \cdot & \cdot & \cdot & \cdot \end{bmatrix}}_{M_{\text{cell}}} \frac{d^2}{dt^2} + \underbrace{\begin{bmatrix} \cdot & \cdot & \cdot & \cdot & \cdot & \cdot & \cdot & \cdot & \cdot \\ \cdot & \cdot & \cdot & \cdot & \cdot & \cdot & \cdot & \cdot & \cdot \\ \cdot & \cdot & \cdot & \cdot & \cdot & \cdot & \cdot & \cdot & \cdot \\ \cdot & \cdot & \cdot & \cdot & \cdot & \cdot & \cdot & \cdot & \cdot \\ \cdot & \cdot & \cdot & \cdot & \cdot & \cdot & \cdot & \cdot & \cdot \\ \cdot & \cdot & \cdot & \cdot & \cdot & \cdot & \cdot & \cdot & \cdot \\ \cdot & \cdot & \cdot & \cdot & \cdot & \cdot & \cdot & \cdot & \cdot \\ \cdot & \cdot & \cdot & \cdot & \cdot & \cdot & \cdot & \cdot & \cdot \\ \cdot & \cdot & \cdot & \cdot & \cdot & \cdot & \cdot & \cdot & \cdot \end{bmatrix}}_{R_{\text{cell}}} \frac{d}{dt} + \underbrace{\begin{bmatrix} \cdot & \cdot & \cdot & \cdot & \cdot & \cdot & \cdot & \cdot & \cdot \\ \cdot & \cdot & \cdot & \cdot & \cdot & \cdot & \cdot & \cdot & \cdot \\ \cdot & \cdot & \cdot & \cdot & \cdot & \cdot & \cdot & \cdot & \cdot \\ \cdot & \cdot & \cdot & \cdot & \cdot & \cdot & \cdot & \cdot & \cdot \\ \cdot & \cdot & \cdot & \cdot & \cdot & \cdot & \cdot & \cdot & \cdot \\ \cdot & \cdot & \cdot & \cdot & \cdot & \cdot & \cdot & \cdot & \cdot \\ \cdot & \cdot & \cdot & \cdot & \cdot & \cdot & \cdot & \cdot & \cdot \\ \cdot & \cdot & \cdot & \cdot & \cdot & \cdot & \cdot & \cdot & \cdot \\ \cdot & \cdot & \cdot & \cdot & \cdot & \cdot & \cdot & \cdot & \cdot \end{bmatrix}}_{K_{\text{cell}}} \right\} \underbrace{\begin{bmatrix} x_1 \\ x_2 \\ x_A \\ x_4 \\ x_5 \\ x_6 \\ x_B \\ x_8 \\ x_9 \end{bmatrix}}_{\mathbf{x}}$$

$$+ Bl \underbrace{\begin{bmatrix} 0 \\ 0 \\ i_A \\ 0 \\ 0 \\ 0 \\ 0 \\ i_B \\ 0 \\ 0 \end{bmatrix}}_{\mathbf{i}} = \underbrace{\begin{bmatrix} -p_1 \\ 0 \\ 0 \\ 0 \\ 0 \\ 0 \\ 0 \\ 0 \\ p_9 \end{bmatrix}}_{\mathbf{p}}$$

The AER control current i used for generating nearest neighbor coupling is defined as:

$$\Rightarrow i_{A(B)} = \frac{S_d}{Bl} \sum_{\mu} c_{\mu} (p_{B(A)})^{\mu} \quad (8)$$

where c_{μ} are the non-linear coupling coefficients of order μ .

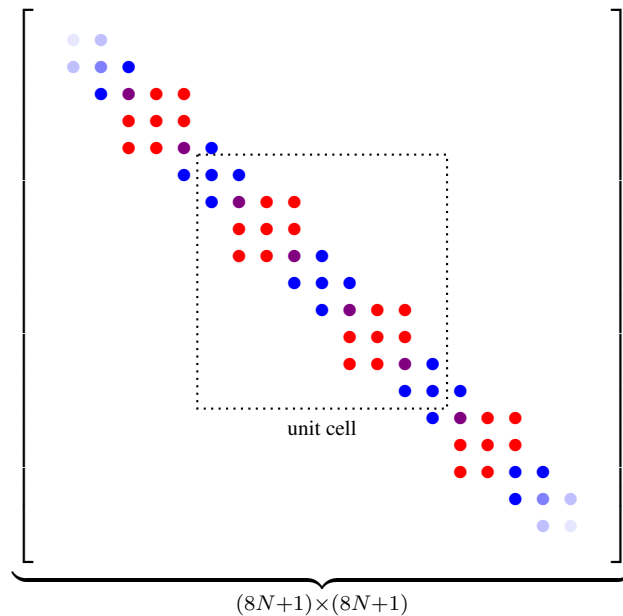
The pressure at the AER is obtained by assuming continuity of pressure:

$$p_A = \frac{1}{C_{aa}} (x_2 - x_A - x_4) \quad (9)$$

$$p_B = \frac{1}{C_{aa}} (x_6 - x_B - x_8)$$

Crystal dynamical matrix:

Finally, an N -cell metacrystal dynamical matrix is built by simply concatenating the unit cell dynamical matrices $M_{\text{cell}}, R_{\text{cell}}, C_{\text{cell}}$,



and numerical simulations can be straightforwardly carried out by Runge-Kutta iterative methods. We have used Verner's "most robust" Runge-Kutta 9(8) pair with an 8th-order continuous extension (43).

Acknowledgements

This research was supported by the Swiss National Science Foundation under Grant No. 200020_200498.

References and Notes

1. J. E. Moore, *Nature* **464**, 194 (2010). Publisher: Nature Publishing Group.
2. P. J. Westervelt, *The Journal of the acoustical society of America* **35**, 535 (1963). Publisher: Acoustical Society of America.

3. S. Le Fouest, K. Mulleners, *Nature Communications* **15**, 2770 (2024). Publisher: Nature Publishing Group.
4. X. Guo, H. Lissek, R. Fleury, *Communications Physics* **6**, 1 (2023). Publisher: Nature Publishing Group.
5. Y. Hadad, J. C. Soric, A. B. Khanikaev, A. Alù, *Nature Electronics* **1**, 178 (2018). Publisher: Nature Publishing Group.
6. F. Zangeneh-Nejad, R. Fleury, *Physical Review Letters* **123**, 053902 (2019). Publisher: American Physical Society.
7. D. A. Dobrykh, A. V. Yulin, A. P. Slobozhanyuk, A. N. Poddubny, Y. S. Kivshar, *Phys. Rev. Lett.* **121**, 163901 (2018). Publisher: American Physical Society.
8. Y. Wang, L.-J. Lang, C. H. Lee, B. Zhang, Y. D. Chong, *Nature Communications* **10**, 1102 (2019). Publisher: Nature Publishing Group.
9. M. Serra-Garcia, R. Süsstrunk, S. D. Huber, *Physical Review B* **99**, 020304 (2019). Publisher: American Physical Society.
10. D. Smirnova, D. Leykam, Y. Chong, Y. Kivshar, *Applied Physics Reviews* **7**, 021306 (2020).
11. L. J. Maczewsky, *et al.*, *Science* **370**, 701 (2020). Publisher: American Association for the Advancement of Science.
12. S. Mukherjee, M. C. Rechtsman, *Science* **368**, 856 (2020). Publisher: American Association for the Advancement of Science.
13. Z. Hu, *et al.*, *Light: Science & Applications* **10**, 164 (2021). Publisher: Nature Publishing Group.

14. D. D. J. M. Snee, Y.-P. Ma, *Extreme Mechanics Letters* **30**, 100487 (2019).
15. P.-W. Lo, *et al.*, *Physical Review Letters* **127**, 076802 (2021). Publisher: American Physical Society.
16. R. Chaunsali, G. Theocharis, *Physical Review B* **100**, 014302 (2019). Publisher: American Physical Society.
17. A. Darabi, M. J. Leamy, *Physical Review Applied* **12**, 044030 (2019). Publisher: American Physical Society.
18. R. Chaunsali, H. Xu, J. Yang, P. G. Kevrekidis, G. Theocharis, *Physical Review B* **103**, 024106 (2021). Publisher: American Physical Society.
19. E. Rivet, *et al.*, *Nature Physics* **14**, 942 (2018). Publisher: Nature Publishing Group.
20. S. Xia, *et al.*, *Science* **372**, 72 (2021). Preprint: <https://www.science.org/doi/pdf/10.1126/science.abf6873>.
21. M. Padlewski, M. Volery, R. Fleury, H. Lissek, X. Guo, *Physical Review Applied* **20**, 014022 (2023). Publisher: American Physical Society.
22. T. Ozawa, *et al.*, *Reviews of Modern Physics* **91**, 015006 (2019). Publisher: American Physical Society.
23. Y. Hadad, A. B. Khanikaev, A. Alù, *Physical Review B* **93**, 155112 (2016). Publisher: American Physical Society.
24. A. Bisianov, M. Wimmer, U. Peschel, O. A. Egorov, *Physical Review A* **100**, 063830 (2019). Publisher: American Physical Society.

25. D. A. Smirnova, L. A. Smirnov, D. Leykam, Y. S. Kivshar, *Laser & Photonics Reviews* **13**, 1900223 (2019). eprint: <https://onlinelibrary.wiley.com/doi/pdf/10.1002/lpor.201900223>.
26. T. Tuloup, R. W. Bomantara, C. H. Lee, J. Gong, *Physical Review B* **102**, 115411 (2020).
Publisher: American Physical Society.
27. M. S. Kirsch, *et al.*, *Nature Physics* **17**, 995 (2021). Publisher: Nature Publishing Group.
28. B.-U. Sohn, *et al.*, *Nature Communications* **13**, 7218 (2022). Publisher: Nature Publishing Group.
29. B. M. Manda, V. Achilleos, O. Richoux, C. Skokos, G. Theocharis, *Physical Review B* **107**, 184313 (2023). Publisher: American Physical Society.
30. R. Chaunsali, P. G. Kevrekidis, D. Frantzeskakis, G. Theocharis, *Physical Review E* **108**, 054224 (2023). Publisher: American Physical Society.
31. L. D. Landau, V. L. Ginzburg, *Zh. Eksp. Teor. Fiz.* **20**, 1064 (1950).
32. V. L. Ginzburg, *Sov. Phys. - Dokl. (Engl. Transl.); (United States)* **2:4** (1956).
33. E. Schrödinger, *Physical Review* **28**, 1049 (1926). Publisher: American Physical Society.
34. D. Zhao, M. Xiao, C. W. Ling, C. T. Chan, K. H. Fung, *Phys. Rev. B* **98**, 014110 (2018).
Publisher: American Physical Society.
35. F. Zangeneh-Nejad, R. Fleury, *Nature Communications* **10**, 1 (2019). Publisher: Springer
US ISBN: 4146701910.
36. A. Coutant, *et al.*, *Physical Review B* **103**, 224309 (2021). Publisher: American Physical Society.

37. N. Kaina, R. Fleury, *Phys. Rev. B* **102**, 134303 (2020). Publisher: American Physical Society.
38. D. Zhao, X. Chen, P. Li, X.-F. Zhu, *AIP Advances* **11**, 015241 (2021).
39. W. P. Su, J. R. Schrieffer, A. J. Heeger, *Physical Review Letters* **42**, 1698 (1979). Publisher: American Physical Society.
40. J. Zak, *Physical Review Letters* **62**, 2747 (1989). Publisher: American Physical Society.
41. M. Barbier, F. M. Peeters, P. Vasilopoulos, J. M. Pereira, *Physical Review B* **77**, 115446 (2008).
42. E. Rivet, S. Karkar, H. Lissek, *IEEE Transactions on Control Systems Technology* **25**, 10.63 (2017). Publisher: Institute of Electrical and Electronics Engineers Place: Piscataway.
43. J. H. Verner, *Numerical Algorithms* **53**, 383 (2010).